ACS APPLIED MATERIALS & INTERFACES

Research Article

www.acsami.org

Bulk Heterojunction Nanomorphology of Fluorenyl Hexa-*peri*-hexabenzocoronene–Fullerene Blend Films

Marina Pfaff,*[,†,‡] Philipp Müller,[†,‡] Pascal Bockstaller,[†] Erich Müller,[†] Jegadesan Subbiah,[§] Wallace Wing Ho Wong,[§] Michael Frédéric Giacomo Klein,[∥] Adam Kiersnowski,[⊥,#] Sreenivasa Reddy Puniredd,[⊥,▽] Wojciech Pisula,[⊥] Alexander Colsmann,[∥] Dagmar Gerthsen,[†,‡] and David John Jones*[,§]

[†]Laboratory for Electron Microscopy, Karlsruhe Institute of Technology (KIT), Engesserstraße 7, 76131 Karlsruhe, Germany

[‡]Center for Functional Nanostructures (CFN), Karlsruhe Institute of Technology (KIT), Wolfgang-Gaede-Str. 1a, 76137 Karlsruhe, Germany

[§]School of Chemistry, Bio21 Institute, University of Melbourne, 30 Flemington Road, Parkville, Victoria 3010, Australia

[∥]Light Technology Institute, Karlsruhe Institute of Technology (KIT), Engesserstraße 13, 76131 Karlsruhe, Germany

[⊥]Max Planck Institute for Polymer Research, Ackermannweg 10, 55128 Mainz, Germany.

[#]Polymer Engineering and Technology Division, Wroclaw University of Technology, Wybrzeze Wyspianskiego 27, 50-370 Wroclaw, Poland

Supporting Information

ABSTRACT: In this study, the nanomorphology of fluorenyl hexa-*peri*-hexabenzocoronene:[6,6]-phenyl C_{61}-butyric acid methyl ester (FHBC:$PC_{61}BM$) absorber layers of organic solar cells was investigated. Different electron microscopical techniques, atomic force microscopy, and grazing incidence wide-angle X-ray scattering were applied for a comprehensive nanomorphology analysis. The development of the nanomorphology upon sample annealing and the associated change of the device performance were investigated. It was shown that the annealing process enhances the phase separation and therefore the bulk heterojunction structure. Due to $\pi-\pi$ stacking, the FHBC molecules assemble into columnar stacks, which are already present before annealing. While the nonannealed sample consists of a mixture of homogeneously distributed $PC_{61}BM$ molecules and FHBC stacks with a preferential in-plane stack orientation, crystalline FHBC precipitates occur in the annealed samples. These crystals, which consist of hexagonal arranged FHBC stacks, grow with increased annealing time. They are distributed homogeneously over the whole volume of the absorber layer as revealed by electron tomography. The FHBC stacks, whether in the two phase mixture or in the pure crystalline precipitates, exhibit an edge-on orientation, according to results from grazing incidence wide-angle X-ray scattering (GIWAXS), dark-field transmission electron microscopy (DF TEM) imaging and selective area electron diffraction (SAED). The best solar cell efficiencies were obtained after 20 or 40 s sample annealing. These annealing times induce an optimized degree of phase separation between donor and acceptor material.

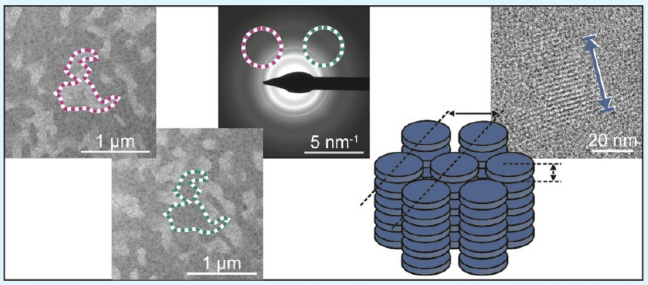

KEYWORDS: *organic solar cells, hexabenzocoronene, electron microscopy, dark-field imaging, EFTEM, electron tomography*

INTRODUCTION

Bulk heterojunction (BHJ) organic solar cells (OSC) are promising photovoltaic devices that can be manufactured at low-cost using roll-to-roll printing methods.[1] The basic operation of BHJ OSCs relies on absorption of light in a blend of donor and acceptor materials. The photogenerated charges form excited states, before being spatially separated and subsequently collected at the electrodes.[2,3] To optimize the BHJ morphology and hence the device performance, it is crucial to gain as much knowledge as possible about the underlying mechanism of device operation. There are many aspects of a BHJ that can affect the overall device performance. These include the individual properties of the materials, such as spectral absorption and charge transport, as well as the compatibility of materials, such as the matching of HOMO and LUMO levels and interface formation. In detailed device studies, often the most elusive parameter that affects the device performance is the nanomorphology of the donor–acceptor blends.

Received: May 28, 2013
Accepted: October 22, 2013
Published: October 22, 2013

Several techniques are available for nanomorphology characterization of BHJ OSCs which contain donor−acceptor blends. Most commonly used is atomic force microscopy (AFM) which provides information on the surface topography but not on the bulk properties of the film. The volume properties of the absorber layers can be studied by transmission electron microscopy (TEM) which comprises several imaging modes to probe different sample properties. While bright-field (BF) TEM is the most common mode to investigate the morphology of BHJ solar cells,[4−8] dark-filed (DF) TEM has been rarely used. This is due to the fact that in general polymers with crystalline structure are usually sensitive to electron irradiation and relatively long exposure times are necessary to record DF TEM images. Only few examples for DF imaging of polymer samples can be found in literature.[9,10] High-resolution TEM (HRTEM) is used to directly image the crystalline structure but its application is restricted by the electron-beam sensitivity of organic materials. Nevertheless, numerous examples of HRTEM investigations of polymers or organic molecules can be found in literature as summarized by Martin et al.[11] Electron energy loss spectroscopy (EELS) and energy-filtered TEM (EFTEM) have been used by several groups to distinguish acceptor and donor domains in BHJ OSCs. The distinction is based on the fact that the plasmon energies of the examined absorber materials differ.[12−14] Low-energy high-angle annular dark-field scanning TEM (HAADF STEM), a technique with sensitive material contrast, was applied for imaging the nanomorphology of poly(3-hexylthiophene):[6,6]-phenyl C_{61}-butyric acid methyl ester (P3HT:$PC_{61}BM$) blends.[15] All standard TEM-based techniques only provide a two-dimensional projection of the examined volume. This limitation can be overcome by TEM tomography which facilitates the reconstruction of the three-dimensional (3D) sample structure. Several examples of 3D reconstructions of the nanomorphology of OSC absorber layers can be found in the literature.[16−19]

X-ray scattering techniques are commonly applied to study the nanomorphology of organic solar cell absorber layers. They provide information about the molecular packing structure, crystallinity, size, and orientation of crystalline domains.[20,21] While small angle X-ray scattering (SAXS) is used to analyze long correlation distances larger than about 10 nm, wide angle X-ray scattering (WAXS) provides information on the order of molecular dimensions.[21] To investigate the crystallinity of surfaces or thin films, grazing incidence wide-angle X-ray scattering (GIWAXS) is a standard method.[22,23] It is, for example, applied to analyze the molecular arrangement of conjugated polymers[22,24,25] and small molecules.[20,26]

In our previous studies, FHBC was employed as electron donor material in BHJ OSCs.[27] Hexa-*peri*-hexabenzocoronene (HBC) is a discotic polycyclic aromatic hydrocarbon with well-known liquid crystalline properties as a result of strong $\pi-\pi$ intermolecular association between the molecules.[27] The columnar $\pi-\pi$ stacking results in high intrinsic charge transport properties, making HBC materials attractive candidates for semiconducting applications.[27] While photovoltaic response of HBC containing devices was first demonstrated in 2001,[28] the introduction of fluorene substituents on the HBC molecule resulted in a material that showed a promising device performance in combination with the fullerene electron acceptor $PC_{61}BM$.[27] Despite the restricted spectral absorption of this FHBC material with absorption onset at 450 nm, power conversion efficiencies (PCEs) of up to 1.5 % were recorded for these FHBC:$PC_{61}BM$ devices with a maximum external quantum efficiency of 40 % at 400 nm.[27] Perhaps, the most interesting aspect of the device characteristics was the high fill factor (FF) of up to 65%. The high FF value indicated that the transport of holes and electrons through the BHJ film is well-balanced as was confirmed in charge mobility measurements.[27,29] The charge transport in BHJ films is determined by the intrinsic mobility of the individual donor and acceptor components as well as the nanomorphology created from the phase separation of the two materials. From our previous work, phase separation between the FHBC and $PC_{61}BM$ materials was evident from the surface topology of the blend films in AFM experiments.[27] Furthermore, the crystalline structure of pure FHBC was revealed by 2D-wide-angle X-ray scattering (2D-WAXS).[27] The results of this study are summarized in Figure 1. Due to $\pi-\pi$ stacking of planar aromatic FHBC

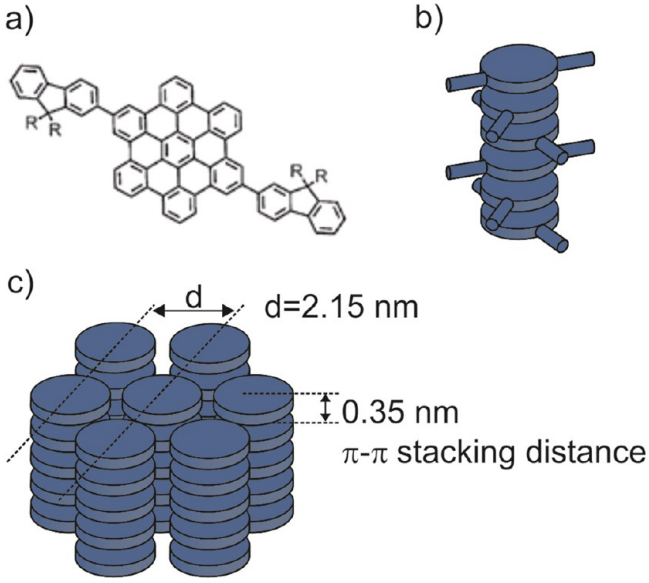

Figure 1. (a) Chemical structure of the FHBC molecule, (b) schematic column of stacked FHBC molecules, and (c) hexagonal arrangement of the columnar stacks.

molecules, self-assembly into columnar stacks occurs as indicated in Figure 1b with a distance of 0.35 nm between single FHBC molecules. The columns can assemble in a hexagonal arrangement, with a plane distance between stacks of 2.15 nm (denoted with d in Figure 1c).

In this study, various electron microscopic techniques, atomic force microscopy (AFM), and grazing incidence wide-angle X-ray scattering (GIWAXS) were applied to study the nanomorphology of FHBC:$PC_{61}BM$ blends before and after annealing. Direct evidence for a pronounced phase separation was obtained, and the assembly of FHBC within the blends is revealed. Good correlation was found between the thermal treatment of the blend films, nanomorphology, and BHJ device performance.

EXPERIMENTAL RESULTS

To thoroughly investigate the nanomorphology of FHBC:$PC_{61}BM$ blends after different annealing times and to correlate the results with the device performance, solar cell devices and BHJ absorber layers with identical processing parameters and annealing treatments were fabricated. The

presentation of the results is accordingly divided into two parts. In the first part the photovoltaic performance of the solar cell devices is presented. The focus of the second part lies on the nanomorphology investigation.

Photovoltaic Performance. The BHJ solar cells were fabricated using FHBC donor and $PC_{61}BM$ acceptor molecules. A schematic diagram of the solar cells with a state-of-the-art device architecture is shown in Figure 2a. On top of a

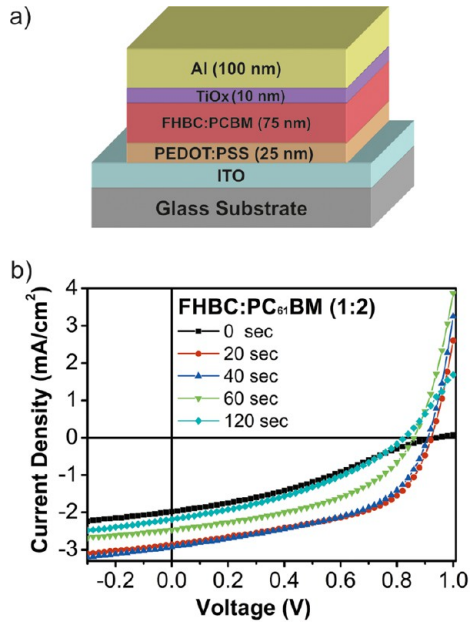

Figure 2. Schematic diagram of the organic solar cells with regular device geometry and (b) $J-V$ characteristics of the FHBC:$PC_{61}BM$ based BHJ solar cells with different annealing times under AM 1.5 G solar illumination, 1000 W/m^2.

structured indium tin oxide (ITO) coated glass slide a 25 nm thin layer of poly(3,4-ethylenedioxythiophene):poly-(styrenesulfonate) (PEDOT:PSS) was deposited. The subsequently deposited 75 nm active layer comprises FHBC and $PC_{61}BM$ (1:2 by wt.). A 10 nm titanium suboxide (TiOx) layer and a 100 nm aluminum layer serve as top electrode. (see Materials and Methods section for details on device fabrication). The $J-V$ characteristics of the devices under illumination after different annealing times are shown in Figure 2b, and the respective photovoltaic key performance data are summarized in Table 1. The FHBC:$PC_{61}BM$ devices annealed for 20 and 40 s at 150 ^{o}C showed the best device performance with PCEs of between 1.30% and 1.35%, respectively. The devices annealed for 0, 60, and 120 s exhibit decreased device performance due to the moderate short circuit current (J_{sc}) and FF. All devices showed a high open-circuit voltage U_{oc}. These results are in agreement with those reported previously.[27] With

Table 1. Photovoltaic Performance of FHBC:$PC_{61}BM$ Solar Cells Depending on Various Annealing Times

annealing time [s]	J_{sc} [mA/cm^2]	V_{oc} [V]	FF [%]	PCE [%]
0	1.96	0.93	33	0.60
20	2.86	0.92	51	1.35
40	2.93	0.90	50	1.30
60	2.47	0.86	45	0.95
120	2.19	0.82	37	0.65

the device results confirmed, the nanomorphology of FHBC:$PC_{61}BM$ blend films was examined.

Nanomorphology. Several electron microscopic techniques (BF TEM and DF TEM, selected area electron diffraction (SAED), EFTEM, TEM tomography), AFM, and GIWAXS were applied to unravel the complex nanomorphology of the FHBC:$PC_{61}BM$ absorber layers and the evolution of the nanomorphology with increasing annealing time.

Figure 3 presents the results for the nonannealed sample. An AFM topography image is presented in Figure 3a, which reveals depressions with a depth of about 10 nm. The depressions are surrounded by elongated structures (marked with black dashed lines). Additional height variations are visible on larger scale, which can be attributed to layer thickness fluctuations. Examples for a higher and a deeper sample region are encircled in Figure 3a.

To analyze the crystalline structure of the sample, SAED patterns were recorded at 200 keV in a transmission electron microscope. Pure FHBC and $PC_{61}BM$ reference samples were additionally examined (data not shown here) to identify the FHBC and $PC_{61}BM$ reflections. FHBC is characterized by two relatively sharp reflection rings which can be assigned to a real space distance of 0.35 nm. The inner ring corresponds to the $\pi-\pi$ stacking distance displayed in Figure 1. The outer ring at 0.175 nm^{-1} is the second order of the inner ring. The reflection rings of pure $PC_{61}BM$ are broad and can be assigned to 0.46, 0.31, and 0.21 nm distances which agree with the results of other groups.[30,31] A diffraction pattern of the nonannealed FHBC:$PC_{61}BM$ layer is presented in Figure 3b, and the corresponding radial intensity line scan in Figure 3c. The diffraction pattern shows three diffuse $PC_{61}BM$ rings with a weak intensity of the two outer rings. One strong and relatively sharp FHBC ring (marked in Figure 3b) is observed while the second ring at 0.175 nm^{-1} is hardly recognizable. The high intensity of the inner ring indicates that FHBC stacks are already present in the nonannealed sample. The absence of further reflections suggests a preferential alignment of the stack axes parallel to the layer which will be denoted as in-plane stack orientation in the following. Moreover, the inner ring intensity changes azimuthally which is indicative for an inhomogeneous in-plane distribution of FHBC stack orientations. For example, the intensity is higher in the upper left and lower right ring segment. To study the origin of the anisotropy of the FHBC ring, DF TEM images were taken with the positions of the aperture indicated by the dashed circles in Figure 3b. Accordingly, mainly electrons from these specific segments of the FHBC ring contribute to the images. The resulting DF TEM micrographs for the two aperture positions are presented in Figure 3d and e which show bright and dark regions with a size of a few 100 nm. The displacement of the aperture position leads to images with essentially complementary contrast. Exemplarily, one grain is marked in both DF TEM images, which appears bright in Figure 3d and dark in Figure 3e. This clearly indicates a preferential in-plane alignment of FHBC stacks, that is, a texture, in regions with a few 100 nm size. A BF TEM image taken at the same sample position as in Figure 3d and e is presented in Figure 3f. None of the large-scale structures of the DF TEM images are visible here; only small-scale structures prevail. The small bright regions can be correlated with regions of smaller sample thickness due to small-size depression which are observed in the AFM image (Figure 3a).

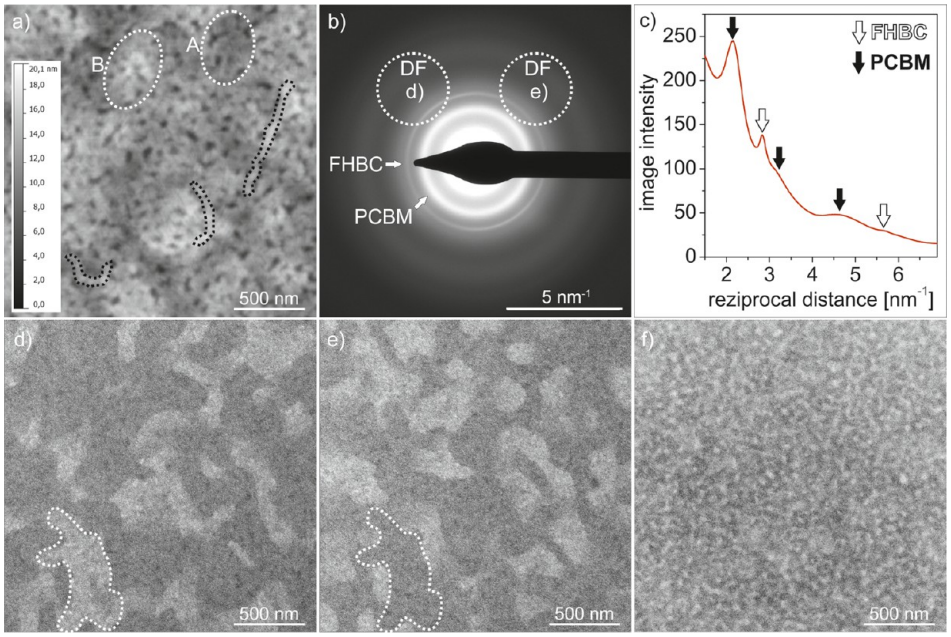

Figure 3. Nanomorphology of the non-annealed FHBC:$PC_{61}BM$ sample. (a) AFM topography image. The dashed white circles mark a deeper (A) and a higher (B) region of the sample. The dashed black lines mark elongated surface structures. (b) TEM diffraction pattern and aperture positions for the DF images (dashed circles). (c) Radial linescan of the diffraction pattern. (d, e) FHBC-sensitive DF TEM images taken at 200 keV corresponding to the aperture positions marked in the diffraction pattern. One grain, which shows contrast inversion, is exemplarily marked in both images. (f) BF TEM image of the same sample position.

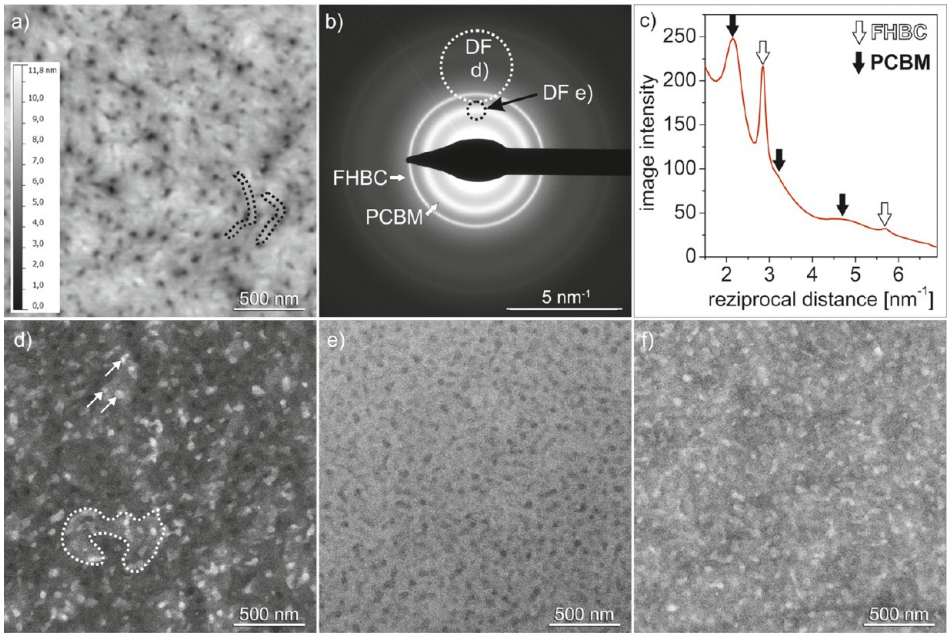

Figure 4. Nanomorphology of the FHBC:$PC_{61}BM$ sample annealed for 120 s. (a) AFM topography image. The dashed black lines mark elongated surface structures. (b) TEM diffraction pattern and aperture positions for the DF images (dashed circles). (c) Radial line scan of the diffraction pattern. (d) DF TEM image taken at 200 keV corresponding to the aperture position on the FHBC ring (marked in b). One grain with the same preferential orientation of the FHBC stacks is encircled. The arrows mark some FHBC precipitates. (e) DF image corresponding to the aperture position on the $PC_{61}BM$ ring (also marked in b) of another sample position. (f) BF TEM image taken at the same sample position as the $PC_{61}BM$-sensitive DF image.

Figure 4 presents results for the sample annealed at 150 °C for 120 s. The nanomorphology of this sample is representative for all annealed samples. The AFM topography image in Figure 4a shows depressions at the surface with sizes which do not depend on the annealing time. Again, elongated structures surrounding the depressions are visible (marked with black dashed lines). In contrast, the large-scale thickness variations disappear almost completely upon annealing (note the different height scale of the two AFM images Figures 3a and 4a).

In Figure 4b and c, a diffraction pattern and the corresponding radial intensity linescan are shown. In comparison to the nonannealed sample, the FHBC $\pi-\pi$

stacking ring exhibits a higher intensity for all annealed samples, indicating a higher degree of crystallinity. Azimuthal intensity variations along the FHBC reflection ring are not observed. However, this does not exclude a preferential FHBC stack alignment because the SAED pattern was taken from a relatively large area, which may contain differently textured grains. Grains with preferentially aligned FHBC stacks are indeed still present as demonstrated by the DF TEM image (Figure 4d) which was taken with the aperture position marked by d) in Figure 4b. In addition, small bright regions with a size of a few 10 nm appear in Figure 4d (marked by arrows) which are absent in the nonannealed samples. The high intensity of these regions suggests crystalline FHBC precipitates. The presence of crystalline FHBC is supported by the high intensity and small width of the FHBC ring in the diffraction pattern (Figure 4b,c) The DF TEM image in Figure 4e was taken with the aperture position shifted to the $PC_{61}BM$ ring. A smaller aperture was chosen to exclude any contribution from FHBC and select only the intensity of the $PC_{61}BM$ ring (see Figure 4b aperture position e). The $PC_{61}BM$-sensitive DF TEM image shows a homogeneous intensity apart from the interspersed dark regions which can be assigned to the FHBC precipitates. Figure 4e suggests that the $PC_{61}BM$ distribution is homogeneous in the phase surrounding the FHBC precipitates. We conclude that a two-phase structure is present after annealing which consists of a FHBC:$PC_{61}BM$ mixture and crystalline FHBC precipitates. Within the FHBC:$PB_{61}CM$ mixture, grains are formed with a preferential alignment of FHBC stacks (marked with a dashed line in Figure 4d). The BF TEM image Figure 4f shows small bright regions which can be correlated with regions of smaller sample thickness. However, the grain structure with preferentially oriented FHBC stacks cannot be visualized by BF TEM.

By comparing FHBC-sensitive DF TEM images of samples with different annealing times (Figure 5), it becomes apparent

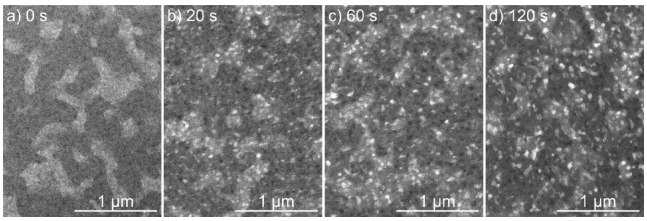

Figure 5. FHBC-sensitive DF TEM images of samples annealed for (a) 0, (b) 20, (c) 60, and (d) 120 s.

that the crystalline FHBC precipitates are formed quickly after only 20 s annealing time. If the annealing time is increased, the FHBC crystallites grow slightly, but the large-scale texture of FHBC stacks in the FHBC:$PC_{61}BM$ mixture remains. To analyze the evolution of the morphology at even longer annealing times, a sample annealed for 5 min was investigated (Supporting Information). The size of the FHBC-rich crystallites further increases as compared to the sample annealed for 120 s and, in addition, large $PC_{61}BM$ crystals with sizes of a few micrometers appear which are surrounded by an FHBC-rich region. The increase of the average FHBC precipitate size is plotted in Figure 6 as a function of the annealing time. It increases from 42 ± 10 nm for 20 s annealing to 83 ± 20 nm for 300 s annealing. The error bar represents the standard deviation of the size distribution.

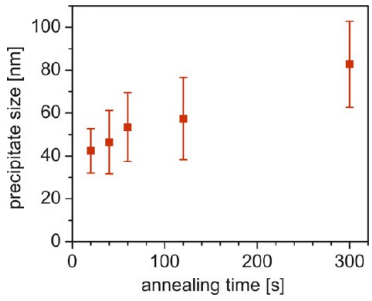

Figure 6. Mean FHBC precipitate size as a function of the annealing time (determined from the FHBC-sensitive DF TEM images). The error bar represents the standard derivation of the size distribution.

A HRTEM image of the sample annealed for 60 s is presented in Figure 7 which is representative for all annealed

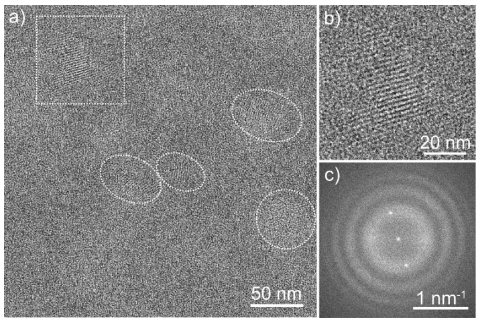

Figure 7. (a) 200 keV HRTEM image of the FHBC:$PC_{61}BM$ sample annealed for 60 s. Crystalline regions are encircled. (b) Enlarged image of the dashed square in the HRTEM image. (c) Fourier transform of HRTEM image.

samples. Lattice fringes are observed in the regions marked by dashed lines in Figure 7a, which are indicative for a crystalline structure. Figure 7b shows the crystalline region in the dashed square with a higher magnification. To determine the distance of the lattice fringes the Fourier transform of this image was calculated (Figure 7c). Two bright spots are visible in addition to the zero-order beam, which correspond to a lattice fringe distance of 2.15 ± 0.15 nm. This distance can be correlated to the lattice plane distance in the hexagonal arrangement of the pure FHBC stacks (Figure1c). A detailed analysis will follow in the Discussion section.

To confirm the interpretation of the images in Figure 4 with respect to the distribution of $PC_{61}BM$ and FHBC, EFTEM was applied. For this purpose, reference electron energy loss (EEL) spectra of pure FHBC and pure $PC_{61}BM$ were recorded which are presented in Figure 8d. The maxima of the plasmon peaks are clearly different for the two materials (FHBC at an energy loss of 22.5 eV, $PC_{61}BM$ at 26.2 eV). This is exploited, to take EFTEM images at different energy losses (Figure 8a–c) to reveal the distribution of FHBC and $PC_{61}BM$. The hatched rectangles in Figure 8d mark the corresponding energy loss windows which were selected with a slit width of 4 eV. The EFTEM image Figure 8a was taken with a slit position centered at an energy loss of 20 eV. For this energy loss, the FHBC signal distinctly exceeds the $PC_{61}BM$ signal, leading to a higher image intensity of the FHBC-rich regions. For the second slit position centered at 23 eV, the two signals have the same intensity, and changes of the image contrast in Figure 8b can be interpreted in terms of thickness variations. The last slit

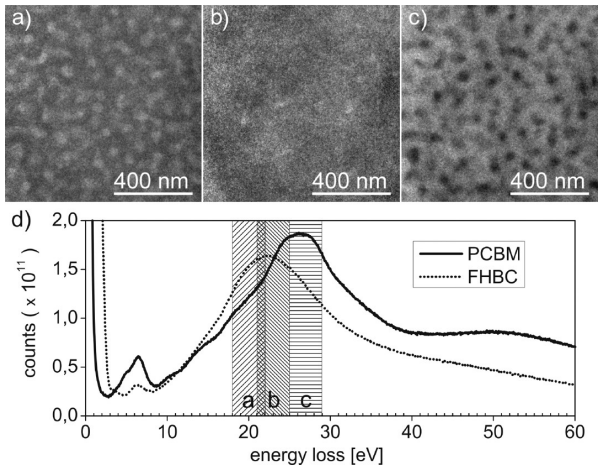

Figure 8. EFTEM images of the FHBC:$PC_{61}BM$ sample annelaed for 60 s. The images are taken with a slit width of 4 eV centered at energy losses of (a) 20 eV, (b) 23 eV, and (c) 27 eV. (d) Low-loss EEL sprectra of pure $PC_{61}BM$ and FHBC. The slit positions for the EFTEM images are marked by the hatched rectancles.

position centered at 27 eV exhibits a higher $PC_{61}BM$ signal. The $PC_{61}BM$-rich phase appears brighter in the EFTEM image Figure 8c. This image closely resembles the $PC_{61}BM$-sensitive DF TEM image (Figure 4e), in which the $PC_{61}BM$ also appears brighter than the FHBC. The comparison of Figure 8a and c shows complementary contrast indicating that small FHBC precipitates are embedded in a FHBC:$PC_{61}BM$ blend.

TEM tomography was applied to analyze the 3D structure of the sample. In Figure 9, three slices extracted from the top

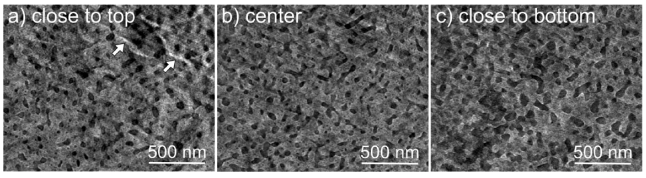

Figure 9. Slices extracted from the TEM tomogram of the sample annealed for 60 s. FHBC precipitates appear dark because the contrast is inverted for better visibility. (a) Slice close to the top, (b) slice from the center, and (c) slice close to the bottom of the sample. The white arrows in (a) indicate elongated surface structures.

(Figure 9a), center (Figure 9b), and bottom (Figure 9c) of the reconstructed volume are shown. FHBC-rich regions appear dark because the image contrast was inverted for improved visibility. The dark FHBC precipitates are distributed homogeneously over the whole sample thickness, but seem to be slightly larger close to the bottom of the sample (Figure 9c). Figure 9a shows a slice close to the sample surface, where bright structures are visible in the upper right corner (marked with arrows). They correspond to the faint elongated structures in the AFM images (Figures 3a and 4a) which surround the depressions. By applying a threshold gray value to the reconstructed volume, the FHBC domains could be extracted and a 3D model of the FHBC distribution was obtained (see video in the Supporting Information). The video confirms that the FHBC domains are homogeneously distributed over the whole volume of the sample.

GIWAXS was performed to study the crystalline organization of the FHBC:$PC_{61}BM$ sample after annealing at 150 °C for up to 120 s. The GIWAXS pattern of the sample before annealing (not presented here) does not exhibit any reflections, indicating none or very poor order on a macroscopic scale (few cm^2) in the probed volume. Figure 10a shows the GIWAXS pattern of a

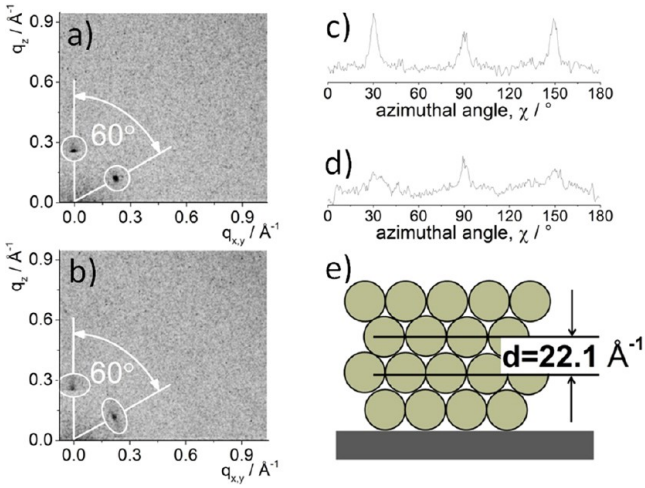

Figure 10. GIWAXS patterns of (a) pure FHBC and (b) FHBC:PC61BM blend (the films were annealing at 150 °C for 120 s prior to measurements). (c, d) Azimuthal intensity distributions within the q-range of 0.282−0.286 for FHBC and FHBC:$PC_{61}BM$ blend respetively. (d) Schematic cross-sectional arrangement of FHBC stacks in the ordered (columnar) phase.

pure annealed FHBC sample which was processed in the same way as the FHBC:$PC_{61}BM$ blend. Three discrete reflections can be recognized in the meridional and off-meridional planes which are characteristic for a hexagonal organization of the columnar stacks with their columnar axes oriented parallel to the surface as illustrated in Figure 10e. The respective distance between the FHBC stack layers corresponds to d = 2.20 nm which agrees well with the lattice fringe distance of 2.15 nm in the HRTEM image of the FHBC:$PC_{61}BM$ blend after annealing (Figure 7). Due to the low crystalline order on a macroscopic scale, only the first order reflections appear without higher order reflections. Reflections from the FHBC $\pi-\pi$ stacking are, however, not observed though confirmed by HRTEM. This observation may indicate that, at the macroscopic scale, hexagonal ordering of the FHBC columns in the films dominates over the $\pi-\pi$ interaction-driven assembly of the FHBC molecules within the columns. The GIWAXS pattern of the FHBC:$PC_{61}BM$ blend (sample annealed for 120 s at 150 °C) (Figure 10b) resembles the GIWAXS pattern of pure FHBC (Figure 10a). However, the azimuthal intensity distribution of the main reflection indicates a decrease of order if $PC_{61}BM$ is added (comparison of Figure 10c and d). This can be concluded from the smearing out of the reflections along the azimuthal angle in Figure 10d, while these reflections are quite sharp for of pure FHBC (Figure 10c). Unfortunately, based on the diffraction data it is not possible to determine the crystallinity degrees of the films. This is mainly due to the fact that there is only one clearly defined scattering peak that describes the ordering just in a single direction of the real space. Moreover, full determination of the amorphous halo in the pattern is not possible due to the limited q-range.

DISCUSSION

Detailed information on the nanomorphology of the FHBC:$PC_{61}BM$ absorber layers and the effect of annealing was obtained by combining several electron microscopic techniques, AFM and GIWAXS. We first focus on the nanomorphology of the FHBC:$PC_{61}BM$ blend before annealing. The images and SAED pattern in Figure 3 demonstrate that the nonannealed sample consists of a homogeneous mixture of $PC_{61}BM$ and FHBC stacks. The FHBC stack axes are preferentially oriented parallel to the substrate with an additional azimuthal texture in regions with a typical size between a few 100 nm and 1 μm. The $PC_{61}BM$ molecules are homogeneously distributed and do not agglomerate to form, for example, pure $PC_{61}BM$ crystallites. This is illustrated in Figure 11a where a scheme of the nanomorphology of the nonannealed FHBC:$PC_{61}BM$ sample is shown.

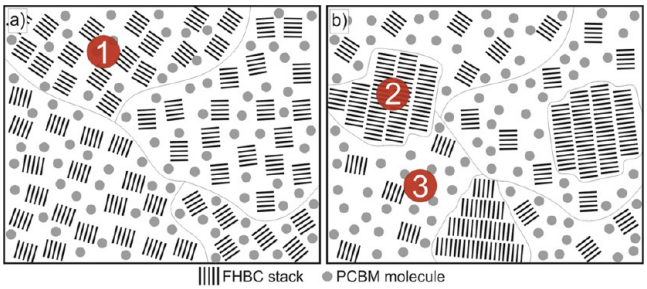

Figure 11. Schematic illustration of the nanomorphology of (a) nonannealed and (b) annealed FHBC:$PC_{61}BM$. Before annealing, the sample consists of a homogeneous mixture of FHBC and $PC_{61}BM$. Grains (1) exist with FHBC stacks which are preferentially aligned parallel to the substrate. During annealing, FHBC crystals are precipitated (2) from the textured FHBC:$PC_{61}BM$ mixture (3).

The morphology of the annealed samples is schematically summarized in Figure 11b. The most notable change of the nanomorphology after annealing consists in the precipitation of crystalline FHBC as demonstrated by the DF TEM (Figures 4d and 5b–d), HRTEM (Figure 7) and the GIWAXS data (Figure 10). The FHBC stacks are arranged in a hexagonal symmetry as indicated in Figures 1c and 10e. The GIWAXS data confirm that the stack axes in the precipitates are indeed preferentially oriented parallel to the substrate (Figure 10b). $PC_{61}BM$-sensitive EFTEM (Figure 8c) and DF TEM images (Figure 4e) reveal a homogeneous distribution of the $PC_{61}BM$ molecules. Furthermore, the FHBC-sensitive DF TEM images (Figure 4d and Figure 5b-d) show that the surrounding FHBC:$PC_{61}BM$ blend contains regions with preferentially aligned FHBC stacks as the non-annealed sample. The size of these regions does not change with increasing annealing time. In contrast, the pure FHBC precipitates grow slightly with increasing annealing time, which becomes apparent in the FHBC-sensitive DF TEM images of the annealing series in Figure 5 and the graph in Figure 6. The growth of the FHBC precipitates leads to an FHBC depletion of the surrounding FHBC:$PC_{61}BM$ blend. For long annealing times (5 min), large $PC_{61}BM$ precipitates are formed which may be initiated by the FHBC depletion of the FHBC:$PC_{61}BM$ blend. The precipitation of large $PC_{61}BM$ crystals has been observed before for long annealing times and high $PC_{61}BM$ concentrations in other $PC_{61}BM$-based absorber layer blends, for example, in P3HT:$PC_{61}BM$ blends.[30,32]

Electron tomography (Figure 9 and Supporting Information) reveals that the FHBC precipitates are homogeneously distributed over the entire sample volume. However, the FHBC precipitate size is slightly larger close to the bottom of the layer which indicates that FHBC precipitation is slightly favored at the interface to the PEDOT:PSS. The annealing process induces only minor changes of the surface topography. The AFM image of the annealed sample (Figure 4a) exhibits the same 10 nm deep depressions as the image of the nonannealed sample (Figure 3a). Only the large-scale thickness variations are reduced.

The nanomorphology of the FHBC:$PC_{61}BM$ blends can be correlated with the photovoltaic performance of the respective solar cells. Annealing of the active layer is required to substantially improve the device power conversion efficiency. The $J-V$ characteristics of the nonannealed devices show pronounced S-shapes. Thermal annealing of the active layer leads to the precipitation of FHBC crystallites. Large PCBM crystals only appear after very long annealing times. The improved morphology leads to better pathways for charge migration, and therefore enhances the device performance. The samples annealed for 20 and 40 s exhibit the best PCE of 1.30% and 1.35%, respectively. This indicates that the absorber layer is sensitive toward small changes of the FHBC precipitate size. A mean size of the crystalline FHBC precipitates in the range of 42–46 nm (obtained after 20 and 40 s of annealing at 150 °C), surrounded by a homogenous mixture of FHBC stacks and $PC_{61}BM$, yields the best exciton dissociation and charge transport among the studied samples. The ideal precipitate size should be in the same range like the exciton diffusion length in this system, which has not been determined yet. However, as this is a baseline study in active layer morphology characterization, the exact value does not appear to be essential at this stage.

The moderate PCE of the cells can be attributed to the FHBC stack orientation "edge-on", that is, parallel to the substrate plane. This orientation is unfavorable for charge transport which preferentially occurs along the FHBC stack axis. Additionally, the insulation side chains of the FHBC molecules impede the charge transport perpendicular to the substrate. The effect of interface modifiers to induce a more favorable organization of the FHBC columns, where the columns are oriented perpendicular, that is, "face-on", to the absorber layer is currently being examined. This orientation would support efficient charge carrier transport to the electrodes.

SUMMARY

The nanomorphology and power conversion efficiency of FHBC:$PC_{61}BM$-based BHJ OSCs was studied and correlated before and after annealing at 150 °C for up to 120 s. FHBC is an interesting donor material for OSCs due to the high fill factor of the solar cells and the possibility for further derivatisation. The application of several electron microscopic techniques, AFM and GIWAXS revealed the complex nanomorphology of the FHBC:$PC_{61}BM$ layers and its dependence on the annealing treatment.

The results of the study can be summarized as follows: (i) The FHBC molecules assemble into columnar $\pi-\pi$ stacks with a distance of 0.35 nm between the FHBC molecules. FHBC stacks are already present before annealing. (ii) The nonannealed sample consists of a mixture of homogeneously distributed $PC_{61}BM$ molecules and FHBC stacks with a

preferential in-plane stack orientation (texture). Strongly textured regions with the same FHBC stack orientation have sizes between a few 100 nm and 1 μm. (iii) During annealing, FHBC crystallites are precipitated from the FHBC:$PC_{61}BM$ mixture. They exhibit the same crystalline structure like pure FHBC, that is, a hexagonal arrangement of the FHCB stacks, with a lattice plane distance of 2.15 nm. (iv) The FHBC precipitates grow with increasing annealing time until the depletion of the FHBC in the mixed phase reaches a critical value and large $PC_{61}BM$ crystals are formed. (v) The FHBC precipitates are distributed homogeneously over the whole volume of the absorber layer as shown by electron tomography. The size of the FHBC precipitates is larger close to the bottom of the layer probably due to preferential FHBC nucleation at the PEDOT:PSS interface. (vi) The best solar cell efficiencies were obtained for samples annealed for 20 and 40 s. This annealing time yields the best donor/acceptor phase separation.

So far, the weak absorption and the orientation of the FHBC stacks parallel to the substrate (edge-on) enable moderate PCEs only. However, with respect to future smart molecule and device design and hence improved absorption and charge carrier transport properties, FHBC will be a promising material class for self-organizing bulk heterojunction solar cells.

MATERIALS AND METHODS

Materials. The synthesis of 2,11-bis(9,9-dioctyl-9*H*-fluoren-2-yl)hexabenzo[bc,ef,hi,kl,no,qr]coronene (FHBC) has been reported previously.[27,33] $PC_{61}BM$ (99.5 %) was purchased from Solenne BV.

Solar Cell Fabrication. Bulk-heterojunction (BHJ) solar cells were fabricated by spin coating 30 nm thick layers of PEDOT:PSS (Clevios AI 4083 from Heraeus) on patterned glass/ITO substrates which were cleaned by acetone, and 2-propanol in an ultrasonication bath and UV/ozone-treated. The PEDOT:PSS films were baked at 140 °C for 10 min in air. A blend of FHBC and $PC_{61}BM$ with a ratio of 1:2 was then spin coated from chlorobenzene solution with a thickness of about 75 nm. A TiO_x precursor solution (1:200 in methanol) was deposited on the active layer by spin coating (2000 rpm) to form a TiO_x layer with a thickness of about 10 nm.[27,34] The films were exposed to air for about 20 min at room temperature for hydrolysis or baked at 150 °C for 20, 40, 60, and 120 s. The films were transferred to a evaporation chamber where aluminum (100 nm) was deposited through a shadow mask (active area: 0.06 cm^2) at approximately 1×10^{-6} Torr. Film thicknesses were determined by Veeco Dektak 150+ Surface Profiler. Current density−voltage (J−V) measurements were carried out with a Keithley 2400 source measurement unit under AM1.5G (1000 W/m^2) illumination from an Oriel solar simulator. The illumination intensity was calibrated using a reference silicon solar cell (PVmeasurements Inc.) certified by the National Renewable Energy Laboratory. Device fabrication and characterizations were performed in an ambient environment without any encapsulation.

For the GIWAXS investigations, the films were spin coated on SiO_2 silicon wafers with a PEDOT:PSS layer.

Sample Preparation for Electron Microscopy Investigations. Samples without a top electrode were prepared under inert conditions for the nanomorphology studies. The PEDOT:PSS layer thickness was slightly increased (~45 nm) to facilitate the dissolution of the layer for TEM sample preparation. The samples were annealed at 150 °C for 20−300 s.

Plan-view samples of the photoactive layers were prepared by the following procedure. First, the absorbing layer on the substrate was cut with a scalpel into small pieces. As PEDOT:PSS is water-soluble, the pieces of the active layer can be floated off the substrate by a drop of water from where they can be transferred onto conventional TEM copper grids. The sample thickness was about 90 nm for all samples as determined by focused-ion-beam cross sections.

Electron Microscopy. TEM images and diffraction patterns were recorded with a Philips CM200 FEG/ST at 200 keV. The EELS, EFTEM, and tomography analyses were performed in an FEI TITAN^3 80-300 instrument at 300 keV. EELS and EFTEM were performed with a Gatan Tridiem 865 HR imaging filter. EEL spectra were recorded with an energy resolution of 0.7 eV and a dispersion 0.05 eV/pixel. A total of 1000 spectra with an exposure time of 0.01 s were acquired and summed up. For the EFTEM images, the exposure time was 4 s, and an energy slit width of 4 eV was chosen.

For tomography, a tilt series of bright-field TEM images was acquired in a tilt-angle range of ±77° in steps of 1° with a "Fischione model 2020" tomography sample holder, resulting in 155 images. For the tilt series acquisition, the software package "FEI Xplore 3D" was used. Subsequent alignment of the image stack and reconstruction of the tomogram were performed with the "FEI Inspect3D V3.0" software. The reconstruction of the tomogram is based on the SIRT algorithm[35] which was performed with 20 iterations. A sectioning of the tomogram's inner structure was obtained by applying a grey-level threshold to the image stack to distinguish between FHBC and $PC_{61}BM$ regions. The "Amira/ResolveRT" software was then used to convert the tomogram into a 3D model.

AFM and GIWAXS. AFM topography images were taken with an Asylum Research MFP-3D in the AC mode.

GIWAXS measurements were performed using an instrument consisting of rotating anode X-ray generator (Rigaku Micromax, operated at 42 kV and 20 mA), Osmic confocal MaxFlux optics, and a three X/Y slit collimation system (JJ X-ray). Samples on the top of approximately 1 × 1 cm^2 silicon platelets were irradiated at the incident angle (α_i) of 0.20°. Diffraction patterns were recorded for 3 h on a MAR345 image plate detector. The camera length (316 mm) and the q-range ($q = 4\pi \sin\theta/\lambda$ = 0.12−2.0 $Å^{-1}$) were calibrated using silver behenate standard. The data was processed and imaged using the Datasqueeze 2.2.9 and Origin 8.6 computer programs.

ASSOCIATED CONTENT

Supporting Information

Electron tomography video and dark-field image of the FHBC:PCBM sample annealed for 300 s. This material is available free of charge via the Internet at http://pubs.acs.org.

AUTHOR INFORMATION

Corresponding Authors

*E-mail: marina.pfaff@kit.edu. Phone: +49 721 6084 8682. Fax: +49 721 60843721. Mailing address: Laboratorium für Elektronenmikroskopie, Engesserstr. 7, Geb. 30.22, R.228, 76131 Karlsruhe, Germany.

*E-mail: djjones@unimelb.edu.au. Phone: +61 3 8344 2371. Fax: +61 3 8344 2384. Mailing address: School of Chemistry, Bio21 Institute, University of Melbourne, 30 Flemington Road, Parkville, Victoria 3010, Australia.

Present Address

$^{\nabla}$S.R.P.: Institute of Materials Research and Engineering, A*Star, 3 Research Link, Singapore, 117602.

Notes

The authors declare no competing financial interest.

ACKNOWLEDGMENTS

This work has been performed within the project F1 of the DFG Research Center for Functional Nanostructures (CFN). It has been further supported by a grant from the Ministry of Science, Research and the Arts of Baden-Württemberg (Az: 7713.14-300). M.F.G.K. is supported by the Karlsruhe School of Optics and Photonics (KSOP). This work is also supported by the Australian Solar Institute (Project Grant 1-GER001 and Fellowship for W.W.H.W.), the Victorian Organic Solar Cell Consortium (www.vicosc.unimelb.edu.au), the Victorian State Government Department of Business Innovation (Victorian

Science Agenda) and Department of Primary Industries (Energy Technology Innovation Strategy), the AAS-BMBF Australia-Germany Solar Photovoltaic Research Exchange Program. Special thanks are given to Professor A. Holmes for generous support of this project. A.K. acknowledges the funding through the statutory subsidy from the Polish Ministry of Science and Higher Education for the Faculty of Chemistry of Wroclaw University of Technology. We further thank Professor U. Lemmer for fruitful discussions and providing the cleanroom lab.

REFERENCES

(1) Krebs, F. C.; Tromholt, T.; Jorgensen, M. *Nanoscale* **2010**, *2*, 873−886.
(2) Brabec, C. J.; Gowrisanker, S.; Halls, J. J. M.; Laird, D.; Jia, S.; Williams, S. P. *Adv. Mater.* **2010**, *22*, 3839−3856.
(3) Günes, S.; Neugebauer, H.; Sariciftci, N. S. *Chem. Rev.* **2007**, *107*, 1324−1338.
(4) Liu, F.; Gu, Y.; Jung, J. W.; Jo, W. H.; Russell, T. P. *J. Polym. Sci., Polym. Phys.* **2012**, *50*, 1018−1044.
(5) Bertho, S.; Oosterbaan, W. D.; Vrindts, V.; D'Haen, J.; Cleij, T. J.; Lutsen, L.; Manca, J.; Vanderzande, D. *Org. Electron.* **2009**, *10*, 1248−1251.
(6) Savenije, T. J.; Kroeze, J. E.; Yang, X.; Loos, J. *Thin Solid Films* **2006**, *511-512*, 2−6.
(7) Vanlaeke, P.; Swinnen, A.; Haeldermans, I.; Vanhoyland, G.; Aernouts, T.; Cheyns, D.; Deibel, C.; D'Haen, J.; Heremans, P.; Poortmans, J.; Manca, J. V. *Sol. Energy Mater. Sol. Cell* **2006**, *90*, 2150−2158.
(8) Abdellah, A.; Virdi, K. S.; Meier, R.; Döblinger, M.; Müller-Buschbaum, P.; Scheu, C.; Lugli, P.; Scarpa, G. *Adv. Funct. Mater.* **2012**, *22*, 4078−4086.
(9) Zhang, X.; Hudson, S. D.; DeLongchamp, D. M.; Gundlach, D. J.; Heeney, M.; McCulloch, I. *Adv. Funct. Mater.* **2010**, *20*, 4098−4106.
(10) Petermann, J.; Moritz, H.; Rieck, U.; Wood, B. A.; Thomas, E. L. *J. Mater. Sci. Lett.* **1989**, *8*, 1023−1025.
(11) Martin, D. C.; Chen, J.; Yang, J.; Drummy, L. F.; Kübel, C. *J. Polym. Sci., Polym. Phys.* **2005**, *43*, 1749−1778.
(12) Drummy, L. F.; Davis, R. J.; Moore, D. L.; Durstock, M.; Vaia, R. A.; Hsu, J. W. P. *Chem. Mater.* **2010**, *23*, 907−912.
(13) Herzing, A. A.; Richter, L. J.; Anderson, I. M. *J. Phys. Chem. C* **2010**, *114*, 17501−17508.
(14) Pfannmöller, M.; Flügge, H.; Benner, G.; Wacker, I.; Sommer, C.; Hanselmann, M.; Schmale, S.; Schmidt, H.; Hamprecht, F. A.; Rabe, T.; Kowalsky, W.; Schröder, R. R. *Nano Lett.* **2011**, *11*, 3099−3107.
(15) Pfaff, M.; Klein, M. F. G.; Müller, E.; Müller, P.; Colsmann, A.; Lemmer, U.; Gerthsen, D. *Microsc. Microanal.* **2012**, *18*, 1380−1388.
(16) van Bavel, S. S.; Sourty, E.; de With, G.; Loos, J. *Nano Lett.* **2009**, *9*, 507−513.
(17) van Bavel, S. S.; Bärenklau, M.; de With, G.; Hoppe, H.; Loos, J. *Adv. Funct. Mater.* **2010**, *20*, 1458−1463.
(18) Andersson, B. V.; Masich, S.; Solin, N.; Inganäs, O. *J. Microsc.* **2012**, *247*, 277−287.
(19) Roehling, J. D.; Batenburg, K. J.; Swain, F. B.; Moulé, A. J.; Arslan, I. *Adv. Funct. Mater.* **2012**, *23*, 2115−2122.
(20) Salleo, A.; Kline, R. J.; DeLongchamp, D. M.; Chabinyc, M. L. *Adv. Mater.* **2010**, *22*, 3812−3838.
(21) Rivnay, J.; Mannsfeld, S. C.; Miller, C. E.; Salleo, A.; Toney, M. F. *Chem. Rev.* **2012**, *112*, 5488−5519.
(22) Perlich, J.; Rubeck, J.; Botta, S.; Gehrke, R.; Roth, S. V.; Ruderer, M. A.; Prams, S. M.; Rawolle, M.; Zhong, Q.; Korstgens, V.; Müller-Buschbaum, P. *Rev. Sci. Instrum.* **2010**, *81*, 105105−105105.
(23) Ruderer, M. A.; Müller-Buschbaum, P. *Soft Matter* **2011**, *7*, 5482−5493.
(24) Sirringhaus, H.; Brown, P. J.; Friend, R. H.; Nielsen, M. M.; Bechgaard, K.; Langeveld-Voss, B. M. W.; Spiering, A. J. H.; Janssen, R. A. J.; Meijer, E. W.; Herwig, P.; de Leeuw, M. *Nature* **1999**, *401*, 685−688.
(25) Kohn, P.; Rong, Z.; Scherer, K. H.; Sepe, A.; Sommer, M.; Müller-Buschbaum, P.; Friend, R. H.; Steiner, U.; Hüttner, S. *Macromolecules* **2013**, *46*, 4002−4013.
(26) Ullah Khan, H.; Li, R.; Ren, Y.; Chen, L.; Payne, M. M.; Bhansali, U. S.; Smilgies, D.-M.; Anthony, J. E.; Amassian, A. *ACS Appl. Mater. Interfaces* **2013**, *5*, 2325−2330.
(27) Wong, W. W. H.; Singh, T. B.; Vak, D.; Pisula, W.; Yan, C.; Feng, X.; Williams, E. L.; Chan, K. L.; Mao, Q.; Jones, D. J.; Ma, C.-Q.; Müllen, K.; Bäuerle, P.; Holmes, A. B. *Adv. Funct. Mater.* **2010**, *20*, 927−938.
(28) Schmidt-Mende, L.; Fechtenkötter, A.; Müllen, K.; Moons, E.; Friend, R. H.; MacKenzie, J. D. *Science* **2001**, *293*, 1119−1122.
(29) Singh, T. B.; Chen, X.; Wong, W. H.; Ehlig, T.; Kemppinen, P.; Chen, M.; Watkins, S.; Winzenberg, K.; Holdcroft, S.; Jones, D. J.; Holmes, A. B. *Appl. Phys. A* **2012**, *108*, 515−520.
(30) Swinnen, A.; Haeldermans, I.; Vanlaeke, P.; D'Haen, J.; Poortmans, J.; D'Olieslaeger, M.; Manca, J. V. *Eur. Phys. J.: Appl Phys.* **2006**, *36*, 251−256.
(31) Ma, W. L.; Yang, C. Y.; Gong, X.; Lee, K.; Heeger, A. J. *Adv. Funct. Mater.* **2005**, *15*, 1617−1622.
(32) Swinnen, A.; Haeldermans, I.; vande Ven, M.; D'Haen, J.; Vanhoyland, G.; Aresu, S.; D'Olieslaeger, M.; Manca, J. *Adv. Funct. Mater.* **2006**, *16*, 760−765.
(33) Jones, D. J.; Purushothaman, B.; Ji, S.; Holmes, A. B.; Wong, W. W. H. *Chem. Commun.* **2012**, *48*, 8066−8068.
(34) Park, S. H.; Roy, A.; Beaupré, S.; Cho, S.; Coates, N.; Moon, J. S.; Moses, D.; Leclerc, M.; Lee, K.; Heeger, A. J. *Nat. Photonics* **2009**, *3*, 297−302.
(35) Gilbert, P. *J. Theor. Biol.* **1972**, *36*, 105−117.